Mon. Not. R. Astron. Soc. **327,** 452–458 (2001)

Instability regions in the upper HR diagram

Cornelis de Jager,[1★] Alex Lobel,[2] Hans Nieuwenhuijzen[1] and Richard Stothers[3]
[1]*SRON Laboratory for Space Research, Sorbonnelaan 2, 3584 CA Utrecht, the Netherlands*
[2]*Harvard-Smithsonian Center for Astrophysics, 60 Garden Street, Cambridge, MA 02138, USA*
[3]*Goddard Institute for Space Studies, NASA, 2880 Broadway, New York, NY 10025, USA*

Accepted 2001 June 6. Received 2001 June 1; in original form 2001 March 20

ABSTRACT

The following instability regions for blueward evolving-supergiants are outlined and compared. (1) Areas in the Hertzsprung–Russell (HR) diagram where stars are dynamically unstable. (2) Areas where the effective acceleration in the upper part of the photospheres is negative, hence directed outward. (3) Areas where the sonic points of the stellar winds (where $v_{\rm wind} = v_{\rm sound}$) are situated inside the photospheres, at a level deeper than $\tau_{\rm Ross} = 0.01$. We compare the results with the positions of actual stars in the HR diagram and we find evidence that the recent strong contraction of the yellow hypergiant HR 8752 was initiated in a period during which $\langle g_{\rm eff}\rangle < 0$, whereupon the star became dynamically unstable. The instability and extreme shells around IRC+10420 are suggested to be related to three factors: $\langle g_{\rm eff}\rangle < 0$; the sonic point is situated inside the photosphere; and the star is dynamically unstable.

Key words: stars: atmospheres – stars: evolution – Hertzsprung–Russell (HR) diagram – stars: interiors – supergiants.

1 INTRODUCTION: HYPERGIANT INSTABILITY

The apparent instability of many stars in the upper part of the Hertzsprung–Russell (HR) diagram has different causes, dependent on the stellar properties, which in turn are partly related to their locations in the HR diagram. Observations obtained in recent years are indicative of various modes of interior or atmospheric instabilities among yellow hypergiants and S Dor stars (luminous blue variables, hereafter LBVs). Evidences for these instabilities in yellow hypergiants were summarized by de Jager (1998). Specifically, they refer to phenomena such as the enormous pulsational amplitude ($\Delta R \simeq 0.25R$) of ρ Cas (Lobel et al. 1997) and the 'bouncing' evolutionary motions of ρ Cas (reviewed by de Jager 1998), of IRC+10420 (Oudmaijer et al. 1994), of Var A in M33 (Humphreys 1975, 1978) and of HR 8752 (de Jager & Nieuwenhuijzen 1997). Another indication of atmospheric instability may be seen in the extended clouds of gas and dust around IRC+10420 (Mutel et al. 1979; Jones et al. 1993; Oudmaijer et al. 1996; Blöcker et al. 1999). In S Dor stars, the large outbursts and the quasi-oscillatory temperature changes (cf. review by van Genderen 2001) have been suggested to be the result of the dynamic instability of the stars (Stothers & Chin 1996). The understanding of the causes of these instabilities may profit from a delineation of areas where one or the other mode of instability prevails.

We summarize earlier work in this field.

Stothers & Chin (1996) showed that in certain areas of the HR diagram, the mean value of $\Gamma_1 [= (\mathrm{d}\ln P/\mathrm{d}\ln\rho)_{\rm ad}]$ can take values below 4/3, which implies dynamic instability of the star. As a consequence, a highly evolved star to which this applies can be triggered to a phase of steady expansion or contraction. Thus, they were able to define two regions of dynamic instability in the upper part of the HR diagram, one for $T_{\rm eff} \leq 10\,000$, another for higher temperatures. These areas were called the 'yellow–red' and the 'blue' dynamic instability regions.

Nieuwenhuijzen & de Jager (1995, summarized by de Jager 1998) outlined two regions in the HR diagram where in the atmospheres of blueward evolving stars, hence very evolved objects, five conditions are obeyed. These are: $g_{\rm eff} < 0.3\,\mathrm{cm\,s^{-2}}$; $\mathrm{d}\rho/\mathrm{d}z < 0$ (z is the vertical ordinate) in the relatively deep parts of the photospheres; the sonic point, i.e. the level where $v_{\rm wind} = v_{\rm sound}$, lies inside the photosphere; the sum $g_{\rm eff} + g_{\rm puls} < 0$ during part of the pulsation; and $\Gamma_1 < 4/3$ in part of the line-forming part of the photosphere. Their two regions were baptised the 'yellow void' and the 'blue instability region'.

In our studies of supergiant instabilities, it became clear to us that it may be possible to advance the understanding of stellar instability (or quasi-instability) by considering the various causes *separately.* To that end, we will delineate the regions in the HR

★E-mail: C.dejager@sron.nl (CdJ)

diagram where supergiants or their atmospheres are unstable in one way or the other.

2 AREAS OF STELLAR DYNAMIC INSTABILITY

Ritter (1879) showed that for radial dynamic stability, the ratio of specific heats γ should exceed the value 4/3. More generally, Ledoux (1958) found that for a real star the first generalized adiabatic exponent Γ_1, suitably averaged, should exceed 4/3 in order that the star be dynamically stable. Following that line, Stothers & Chin (1995) and Stothers (1999) demonstrated that a non-adiabatic, spherically symmetric envelope of a star is dynamically unstable when $\sigma^2 \leq 0$, where σ^2 is the square of the adiabatic eigenfrequency. Here

$$\sigma^2 = \frac{(3\langle\Gamma_1\rangle - 4)\int_r^R P\,\mathrm{d}(r^3)}{\frac{1}{3}\int_r^R r^2\rho\,\mathrm{d}(r^3)}, \quad (1)$$

with

$$\langle\Gamma_1\rangle = \frac{\int_r^R \Gamma_1 P\,\mathrm{d}(r^3)}{\int_r^R P\,\mathrm{d}(r^3)}. \quad (2)$$

The lower bound r of the integration was placed at the bottom of the envelope, which is in all relevant cases deep inside the star, mostly very close in distance to the centre. Formally, it should be placed at the very centre, at $r = 0$, but truncation to a small r value is allowed, because at the base of the envelope the relative amplitude $\delta r/r$ is already many powers of ten smaller than its value at the surface and therefore the deepest regions do not contribute to the stellar (in)stability.

Stothers (1999), Stothers & Chin (2001) gave various examples of the behaviour of stellar models for different values of $\langle\Gamma_1\rangle$. We quote one of them: fig. 2 Stothers & Chin (2001) shows the time-dependent distance from the stellar centre of various layers of a dynamically unstable and pulsationally stable supergiant ($\log L/\mathrm{L}_\odot = 6$; $T_{\rm eff} = 10\,000$). In that case a value $\langle\Gamma_1\rangle = 1.330$ was found, which implies, with equation (1), a negative value of σ^2. Hence, the model should be dynamically unstable, and this is confirmed by the model calculations. An additional result is that the model appears to be pulsationally stable.

Two comments are here in order. First, it appears, from a look at the model calculations given, that stars where $\langle\Gamma_1\rangle <$ or $>$ 4/3 are often also (but in rough approximation only) pulsationally unstable or stable, respectively. Next, one may wonder whether averaging Γ_1 over the *atmosphere only* can also give information on the instability of the whole star, because for the stars situated in the upper part of the HR diagram the atmosphere occupies a considerable fraction of the star. We refer to our Fig. 4 (below) which shows that $\Delta r/R$ (where Δr is the depth range between $\tau_{\rm R} = 0.001$ and 10) attains values of the order of 0.1 to more than 0.3. A comparison with Stothers's model calculations shows that this extent is not large enough, because $\delta r/r$ is still considerable at $\tau_{\rm R} = 10$.

Our main question is that of the delineation of the areas in the HR diagram where $\langle\Gamma_1\rangle < 4/3$. The data for the yellow–red hypergiant region are given in fig. 1 of Stothers & Chin (1996). In that paper, particular attention was given to the high-temperature border line. Its position, depending on the assumed value for the parameter for convective mixing, is given in our Fig. 1. The positions of the lower and upper boundaries of the yellow–red instability area are tentative, being dependent on the uncertain rates of main-sequence and red-supergiant mass loss.

The definition of the blue area is more uncertain. It can be read from Stothers & Chin (1996), where the instability area, for a metal ratio $Z = 0.03$, is displayed in their figs 1 and 2. The red-edge parameters are listed in table 1 of Stothers & Chin (1996). The blue area has a high-luminosity cut-off around $\log(L/\mathrm{L}_\odot) = 6.1$. This value is uncertain; it may be as low as 5.9. The low-luminosity cut-off is around $\log(L/\mathrm{L}_\odot) = 5.4$. The tentative border lines of the blue area are also drawn in our Fig. 1.

An immediate question to deal with in this respect is that of the physical reasons which make $\langle\Gamma_1\rangle < 4/3$ in the two unstable regions and why the stars are stable in between. This is the result of the influence of the partial ionization of hydrogen and helium, and of the influence of radiation pressure. The two regions of instability in the HR diagram represent subsequent phases of stellar evolution. The first effect (partial ionization of H and He) is mainly important in the yellow–red region. The more evolved stars lie in the blue instability region. Since these stars have lost more mass, they possess larger luminosity-to-mass ratios, which increases the relative intensity of radiation pressure in their envelopes. Consequently, their $\langle\Gamma_1\rangle$-values can fall below 4/3, even at rather high temperatures, where the zones of partial ionization of hydrogen and helium are normally too small to be of much importance.

Two aspects are brought forward by Fig. 1: the yellow–red area contains all red and yellow hypergiants. The blue area contains many S Dor stars (LBVs) in their stable states. This is one of the bases for the assumption (Stothers & Chin 1996, in line with Lamers, de Groot & Cassatella 1983) that yellow hypergiants are dynamically unstable stars that are evolving blueward and that, having entered the blue instability region, show up as S Dor stars (LBVs).

This assumption implies that S Dor stars are very evolved, dynamically unstable, stars. The evidence for this relies on atmospheric abundances. He, N and Na overabundance in some yellow hypergiants and S Dor stars (Takeda & Takada-Hidai 1994; El Eid & Champagne 1995) are indicative of nuclear fusion products. The same applies to IRC+10420 (Klochkova, Chentsov & Panchuk 1997; Blöcker et al. 1999). The low masses of IRC+10420 and HR 8752 (Nieuwenhuijzen & de Jager 2000) also suggest that these stars are evolved post-red objects. Hence, S Dor stars ought to be more highly evolved than yellow hypergiants.

3 PHOTOSPHERIC INSTABILITY DEFINED BY $g_{\rm eff} < 0$: THE CASE OF HR 8752

In order to study photospheric instability, we have calculated photospheric models and derived from these models the four components of the acceleration: the Newtonian acceleration, $g_{\rm N}$; the radiative value, $g_{\rm r}$; the turbulent acceleration, $g_{\rm t}$; and the acceleration due to the wind, $g_{\rm w}$. They add up to $g_{\rm eff}$. For stars with $T_{\rm eff}$ below roughly 10 000 K, the turbulent and Newtonian components are the most important ones; for hotter stars $g_{\rm r}$ contributes too, and for the hottest and most luminous ones $g_{\rm w}$ becomes a major component. Cases can occur in which their sum, $g_{\rm eff}$, is negative, hence directed outward. For cool stars, $g_{\rm N}$ and $g_{\rm t}$ are the competing components. Actually, for the most luminous cool objects the absolute value of $g_{\rm t}$ can exceed that of $g_{\rm N}$, and in that case $g_{\rm eff}$ will be directed outward. (See Table 1, below.)

For the computations, the input parameters of the models are as follows (apart from $L/\mathrm{L}_\odot$ and $T_{\rm eff}$).

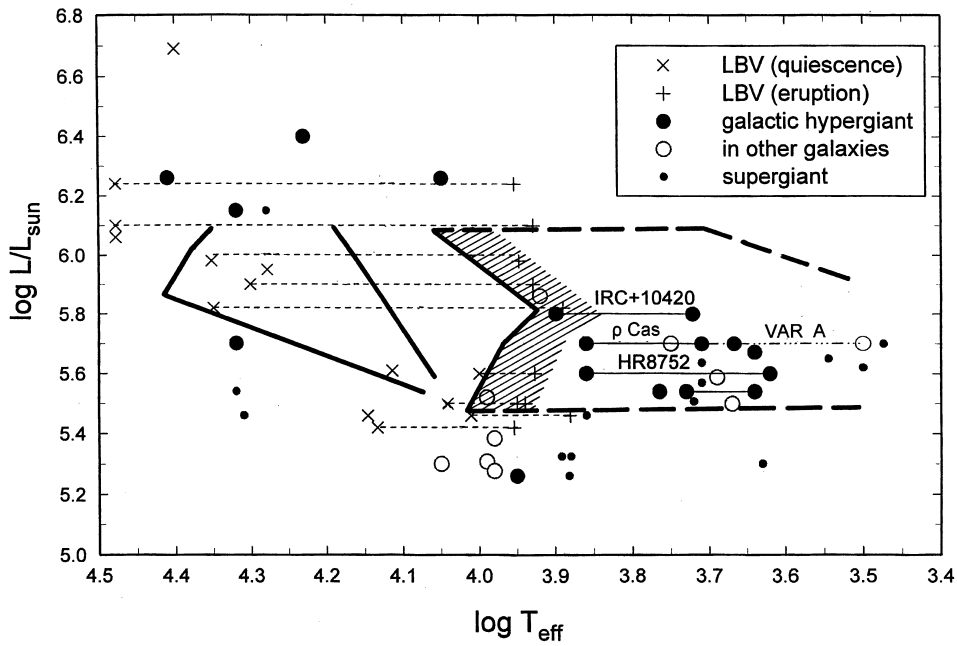

Figure 1. Areas in the upper part of the HR diagram where stars are dynamically unstable according to the criterion $\langle\Gamma_1\rangle < 4/3$. The diagram shows the 'yellow–red' and the 'blue' dynamic instability regions. No model calculations are so far available above and below the upper and lower dashed horizontal lines, respectively.

Table 1. The components of $g_{\rm eff}$ at an optical depth of $\tau_{\rm R} = 0.1$ in photospheres defined by some combinations of $T_{\rm eff}$ and $\log(L/{\rm L}_\odot)$, the latter written in the table heading as L. The table also gives the corresponding stellar mass $M/{\rm M}_\odot$ (written in the heading as M) for blueward evolution, the corresponding rate of mass loss $-\log\dot{M}$ (written as $\dot{M}$), and the assumed microturbulent velocity component ζ_μ. M, $\dot{M}$ and ζ_μ were derived as described in the text. The microturbulence is in km s^{-1} and the accelerations in cm s^{-2}.

$T_{\rm eff}$	L	M	$\dot{M}$	ζ_μ	$g_{\rm N}$	$g_{\rm r}$	$g_{\rm t}$	$g_{\rm w}$	$g_{\rm eff}$
7079	5.45	7.91	4.86	4.94	1.68	−.02	−.32	0	1.34
7079	6.05	34.60	3.32	4.81	1.87	−.02	−.37	0	1.48
7943	5.35	7.50	5.17	15.25	2.55	−.13	−.78	0.01	1.65
7943	5.7	13.1	4.47	7.48	2.31	−.12	−.54	0.01	1.66
10000	6.0	32.7	4.94	20.11	7.55	−.76	−4.80	0.05	2.04
15850	5.7	19.8	5.24	13.80	35.0	−3.6	−.7	1.3	32.0

(i) The stellar mass, $M/{\rm M}_\odot$. This value is derived from Maeder & Meynet (1988). We used their masses for blueward evolving stars. An interpolation programme was developed to obtain $M/{\rm M}_\odot$ for input $L/{\rm L}_\odot$ and $T_{\rm eff}$ values.

(ii) The stellar rate of mass loss, $\dot{M}$. These values were taken from de Jager, Nieuwenhuijzen & van der Hucht (1988). We realize that some authors advocate the use of higher values of $\dot{M}$ for the most luminous stars (factors of 2 and even 3 are sometimes mentioned) but we decided to use values from the published data for the sake of consistency, and also because there are no compelling observational reasons yet that suggest higher values of $\dot{M}$. As it happens, the value of $g_{\rm w}$, which depends on $\dot{M}$, is in no case a decisive contributor to $g_{\rm eff}$.

(iii) The microturbulent velocity component in the line-of-sight, ζ_μ. This quantity is unknown over the greater part of the HR diagram. Since input data are needed for a consistent photospheric model, we had a look at the literature and compared the observationally derived ζ_μ values with the photospheric sound velocity $v_{\rm s}$ at $\tau_{\rm R} = 0.67$. We found for the ratio $\zeta_\mu/v_{\rm s}$ values ranging between 1.4 and 2.2, and clustering around 2. Therefore we decided to make the computations for two cases: $\zeta_\mu = v_{\rm s}$ (in order to have a 'minimum case') and $\zeta_\mu = 2v_{\rm s}$, which may be more than a maximum case for the most luminous hot stars, because for such stars, for which the sonic point is situated in photospheric regions (see Fig. 3, below), the large observed ζ_μ-value is partly a result of the strong $v(\tau)$ gradient over the region of line formation, and the real value of ζ_μ is therefore smaller. An example is the B2 supergiant HD80077 (Carpay et al. 1989) for which $\zeta_\mu = 23\,{\rm km\,s^{-1}}$. For cooler and less luminous stars $\zeta_\mu = 2v_{\rm s}$ is a valid approximation.

The various accelerations were derived on the basis of the equation of conservation of momentum, written as

$$\frac{-\,{\rm d}P_g}{\rho\,{\rm d}z} = \frac{GM}{r^2} + g_{\rm r}(r) + \frac{{\rm d}(v_{\rm w})^2}{2\,{\rm d}z} + \frac{(\zeta_\mu)^2\,{\rm d}\ln\rho}{2\,{\rm d}z}. \qquad (3)$$

Strictly speaking, this equation only applies to stationary situations. However, it may also apply to the stellar wind during outbursts, when these are well underway, because an average outburst lasts for about ten or more dynamic time-scales.

Therefore, the stationary wind approximation may be acceptable in most cases.

In equation (3) we write

$$g_{\rm r} = \frac{1}{\rho}\frac{{\rm d}P_{\rm r}}{{\rm d}z}, \tag{4}$$

where

$$P_{\rm r} = \frac{1}{c}\int I_\omega \cos^2\theta \, {\rm d}\omega. \tag{5}$$

Further,

$$v_{\rm w} = \frac{-\dot{M}}{4\pi r^2 \rho}. \tag{6}$$

Equation (3) is finally written as

$$g_{\rm eff} = g_{\rm N} + g_{\rm r} + g_{\rm w} + g_{\rm t}, \tag{7}$$

which defines the four components and their sum. All five quantities are depth dependent, and not to a small degree: Cases are rare in which $g_{\rm eff}$ varies by less than a factor of 2 over the photosphere, and there are many cases in which the range is larger than a factor of 10. Evidently, the structure of a photosphere in which $g_{\rm eff}$ varies over such a large range differs greatly from one in which it is constant with depth.

To illustrate the relative importance of the g-components for various combinations of $T_{\rm eff}$ and $L/{\rm L}_\odot$, we refer to Table 1.

In view of the strong variability of $g_{\rm eff}(\tau)$, the photospheric models were derived by an iterative method. With the above input values and with an estimated initial value for $g_{\rm eff}$ [we took $(g_{\rm eff})_{\rm in} = g_{\rm N} + g_{\rm r}$ at $\tau = 0.67$], a photospheric model was interpolated in the Kurucz set of models. For that model the depth dependent values of $g_{\rm eff}$ were calculated.

The next step was a calculation of a model with these depth-dependent $g_{\rm eff}(\tau)$ values, on the basis of a $T(\tau)$ relation interpolated in the Kurucz models for the given value of $T_{\rm eff}$ and the average $g_{\rm eff}$ value. For the new model, $g_{\rm eff}(\tau)$ was derived again, and a new (third approximation) model with depth-dependent $g_{\rm eff}(\tau)$ was derived; a process that was repeated until convergence was reached, in the sense that the new $\langle g_{\rm eff}(\tau)\rangle$ did not differ significantly from that of the previous step.

For low values of $T_{\rm eff}$, roughly for $T_{\rm eff} < 10\,000$ K, convergence was normally reached in three to five iterations, as is shown in the example of Table 2. As a rule we stopped after the fourth or fifth iteration. For higher temperatures, where all four g components come into play, successive iterations appear to alternate around an average value, as is shown in the example of Table 3. We checked that this average is close to the 'best' value and therefore, starting with the fourth iteration, we usually took as input parameters for the 2nth iteration the average values of $g_{\rm eff}(\tau)$ between those of the $(2{\rm n}-1)$th and the $(2{\rm n}-2)$th iterations. This procedure worked well.

For the resulting model, two values for the average of $g_{\rm eff}$ were derived. The first, called $\langle g_{\rm eff}\rangle$, is the average over the depth interval $\tau = 0.007$ to 0.75; the other, $\langle g_{\rm eff}\rangle_{\rm out}$ was averaged over a more distant region: 0.007 to 0.2. There are models for which the latter is negative while the former is not. These models thus define a transition region between models for which the average $g_{\rm eff}$ values are positive and negative respectively. That transition region is too thin to make it well visible in Fig. 2.

Note in Fig. 2 the position of the region with $\langle g_{\rm eff}\rangle < 0$. It strikes us that the three stars mentioned earlier (ρ Cas, HR 8752 and IRC+10420) are all situated close to the line $\langle g_{\rm eff}\rangle = 0$. IRC+10420 even lies in the region of negative values. This suggests that the low-temperature border line of the area where $\langle g_{\rm eff}\rangle \leq 0$ is an obstacle for blueward-moving supergiants. This observation implies that the hypergiant characteristics are (at least partly) related to their positions in and near that instability area. Earlier, two of us (de Jager & Nieuwenhuijzen 1997) described the repeated to-and-fro movements of HR 8752 along the $T_{\rm eff}$ axis as 'bouncing against the border of the instability region'. Fig. 2 specifies the location of the bouncing as the low-$T_{\rm eff}$ border of the area where $g_{\rm eff} < 0$. The object HR 8752 is remarkable in that respect. Starting around the years 1983–1985, its $T_{\rm eff}$ value has steadily and dramatically increased till about the year 1998 (Israelian, Lobel & Schmidt 1999), which implies a steady compression, reminiscent of a dynamic instability (Nieuwenhuijzen & de Jager 2000; de Jager et al. 2001). This behaviour can be interpreted as a dynamic instability triggered by the decrease of $\langle g_{\rm eff}\rangle$ to below zero. Indeed, $\langle g_{\rm eff}\rangle < 0$ the last time in 1978. That period was followed by one of enhanced mass loss (around 1980–1982), and that event was followed, starting in the period 1983–1985, by the long period of $T_{\rm eff}$ increase.

Table 2. A typical course of the iterations for a model with low $T_{\rm eff}$. Here, $\tau_{\rm son}$ is the optical depth of the sonic point, $\langle g_{\rm eff}\rangle$ is the average value of $g_{\rm eff}$ over the $\tau_{\rm R}$ interval between 0.007 and 0.75, and $\langle g_{\rm eff}\rangle_{\rm out}$ is the average over the depth region 0.007 to 0.2. The model is for $T_{\rm eff} = 7079$ K and $\log(L/{\rm L}_\odot) = 5.9$; $\zeta_\mu = 4.87\,{\rm km\,s^{-1}}$.

iteration #	$\tau_{\rm son}$	$\langle g_{\rm eff}\rangle$	$\langle g_{\rm eff}\rangle_{\rm out}$
1	–	0.79	0.79
2	.0017	1.55	1.46
3	.0007	1.44	1.29
4	.0007	1.47	1.34
5	.0007	1.46	1.33

Table 3. As Table 2, but for a higher temperature. $T_{\rm eff} = 15\,850$ K and $\log(L/{\rm L}_\odot) = 5.7$; $\zeta_\mu = 13.8\,{\rm km\,s^{-1}}$.

iteration #	$\tau_{\rm son}$	$\langle g_{\rm eff}\rangle$	$\langle g_{\rm eff}\rangle_{\rm out}$
1	–	90	90
2	.29	56	53
3	.004	22	11
4	.11	34	22
5	.012	48	42
6	.007	38	29
7	.012	49	44
8	.007	36	28

4 THE DEPTH OF THE SONIC POINT

Along the lines described in the previous section, we derived the optical depth $\tau_{\rm son}$ where the wind velocity equals that of sound. Fig. 3 gives lines in the HR diagram of constant $\tau_{\rm son}$ values, again for the two assumed values for ζ_μ. We draw attention to the position of IRC+10420 and the neighbouring hypergiant HD 33579 (open circle in the diagrams). The latter star cannot be used

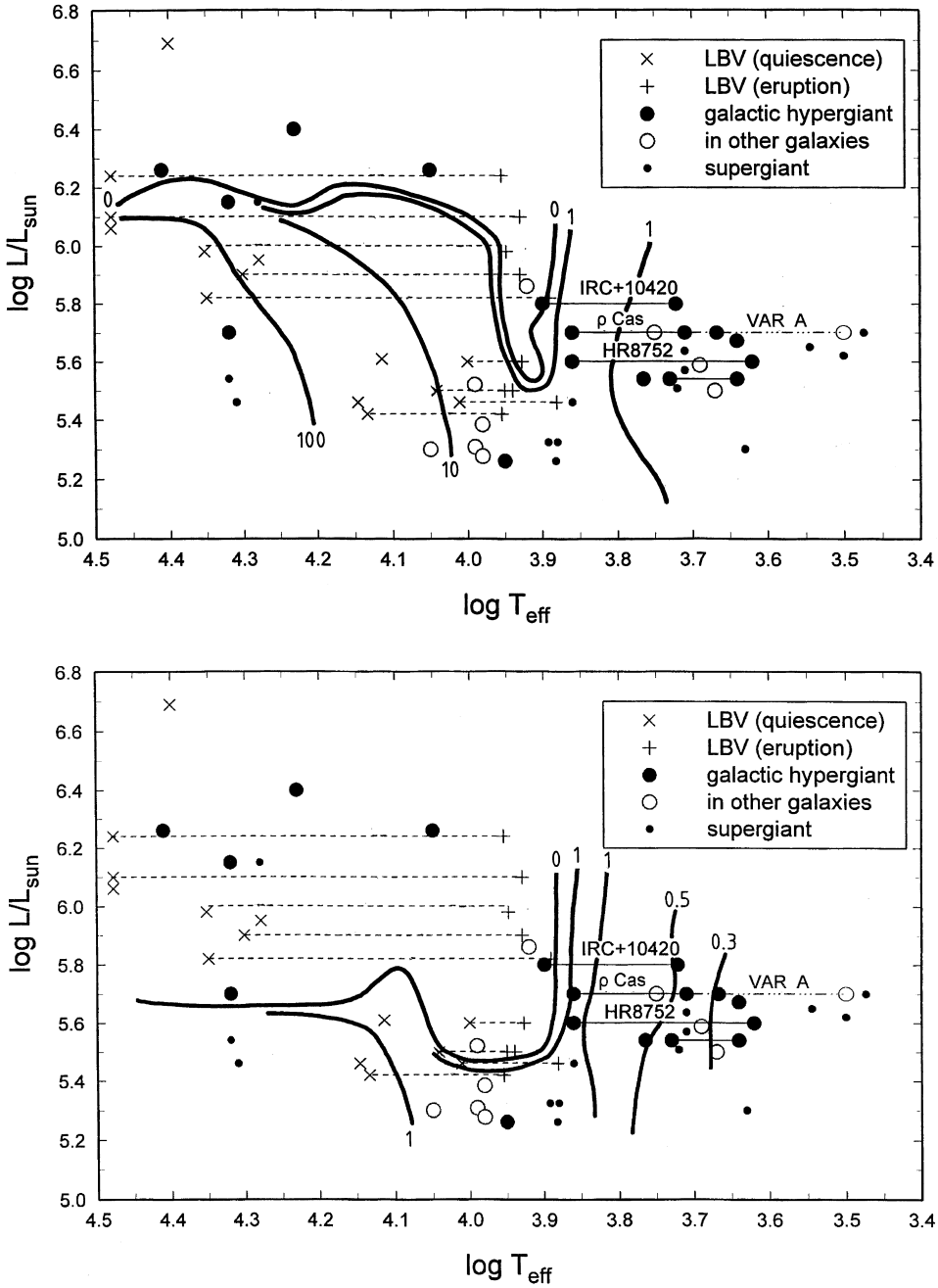

Figure 2. The HR diagram with lines of equal $\langle g_{\rm eff}\rangle$ values. The upper diagram is for $\zeta_\mu = v_{\rm s}$; the other is for twice these values.

to check the results of Fig. 3, because it is a redwards-evolving star, as follows from its chemical abundances (Humphreys, Kudritzki & Groth 1991), and from its large mass (Nieuwenhuijzen & de Jager 2000). The other object, however, IRC+10420, is an evolved post-red star, as noted in Section 2. It is evolving blueward: its spectral type changed from F8 I^+ in 1973 to mid-A in 1998. Hence its effective temperature has increased by about 2000 K in these 26 yr. This instability may be the result of a combination of three causes: The star is located at the boundary of the $\langle g_{\rm eff}\rangle < 0$ area and inside the $\tau_{\rm son} > 0.01$ area, a limit that roughly defines the cool edge of the instability region for hot, radiatively driven winds. Also, the object is dynamically unstable (cf. Fig. 1). These effects may explain the instability and the large surrounding gas clouds. Blöcker et al. (1999) suggest that a phase of heavy mass loss occurred some 60 to 90 yr ago.

One aspect of the large $\tau_{\rm son}$ values is that the replacement time $t_{\rm repl}$ of the photosphere is relatively short. We estimate it at $H/v_{\rm s}$ where H is the scaleheight. Inserting the expressions for the two variables and taking μ and γ equal to unity (for order-of-magnitude considerations), one obtains $t_{\rm repl} = (\mathcal{R}T_{\rm eff})^{1/2}/g_{\rm eff}$. For a star with $T_{\rm eff} = 10\,000$ K and $g_{\rm eff} = 1$ we have $t_{\rm repl} = 10$ d.

A related matter is that of the relative extent of the photospheres. To get an impression, we calculated for a number of the model atmospheres the value of $\Delta r/R$, where r is the radial distance between the levels with $\tau_{\rm R} = 0.001$ and 10. The outcome is presented in Fig. 4. It appears that for the three unstable yellow

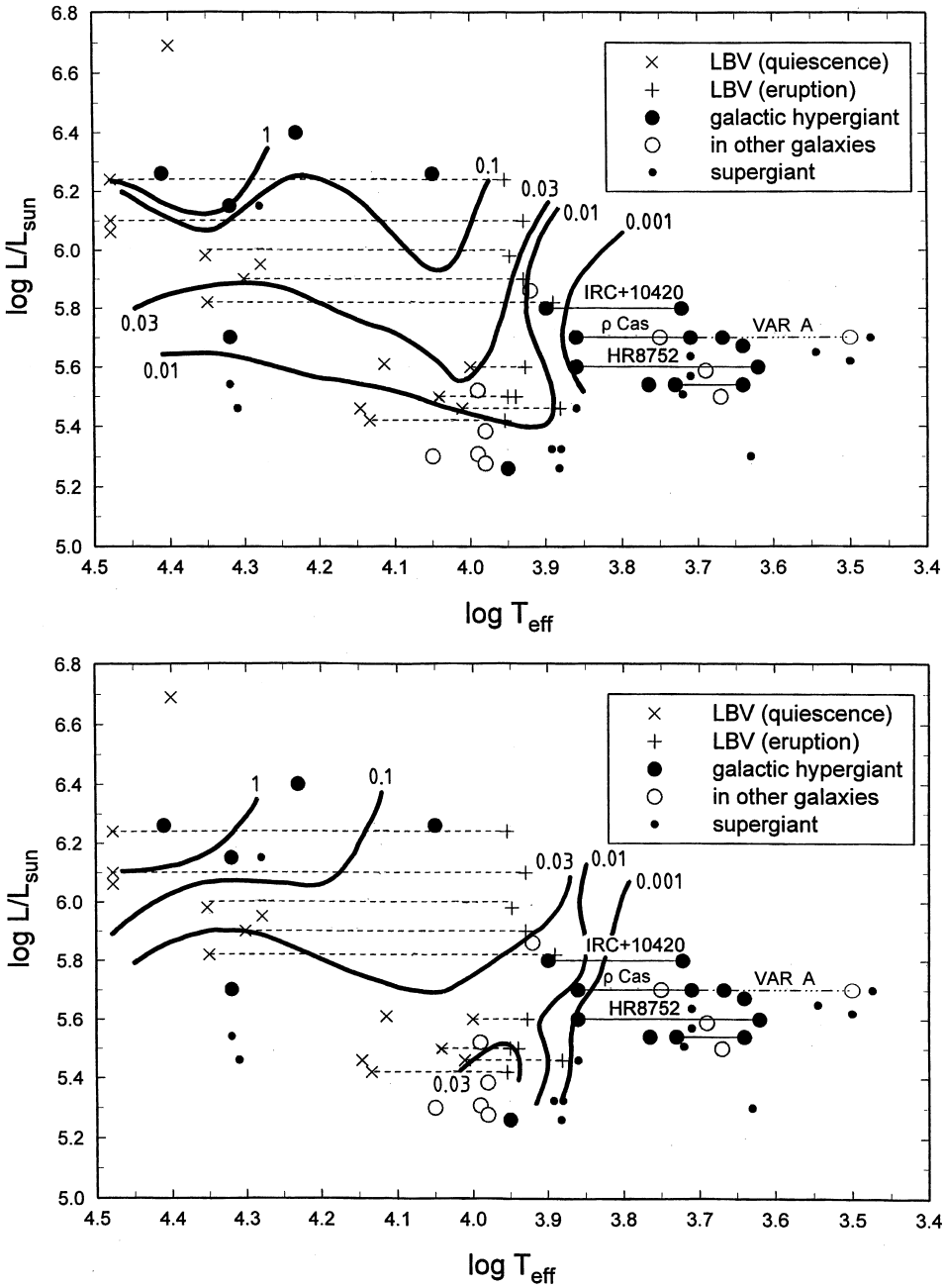

Figure 3. The HR diagram with lines of equal τ_{son} values. The upper diagram is for $\zeta_\mu = v_s$ at $\tau_R = .67$. The lower one is for twice these values.

hypergiants that were mentioned several times in this paper, the relative extent of the photosphere is larger than 0.3, a considerable fraction of the star.

5 CONCLUSIONS

The main results of this study are contained in Figs 1–3. They demonstrate the presence of two regions of stellar interior dynamic instability, one in the yellow–red and another in the blue part of the HR diagram. In addition, it appears that the atmospheres of blueward-evolving supergiants become unstable when their effective temperature has risen to about 8000 K, for two reasons: the average g_{eff} value becomes negative, and the sonic point is getting situated in photospheric regions.

We have compared these results with the recent life histories of two yellow hypergiants, HR 8752 and IRC+10420, and we have shown that their behaviour can be explained on the basis of the data presented in this paper.

The three instability criteria discussed here are not closely related to each other, but their main implication is that these instabilities can amplify each other when they overlap. All of them are useful in explaining stellar instability and high mass loss. The two areas in the HR diagram defined by $\langle g_{eff} \rangle < 0$ and by $\tau_{son} > 0.01$ differ in shape and position from the 'yellow void' and the 'blue instability region', as described in Section 1. That is because these latter two regions were defined according to a combination of criteria. We think that the present study does not invalidate the earlier results, but that there is merit in pursuing more specific studies of atmospheric instability, as started here.

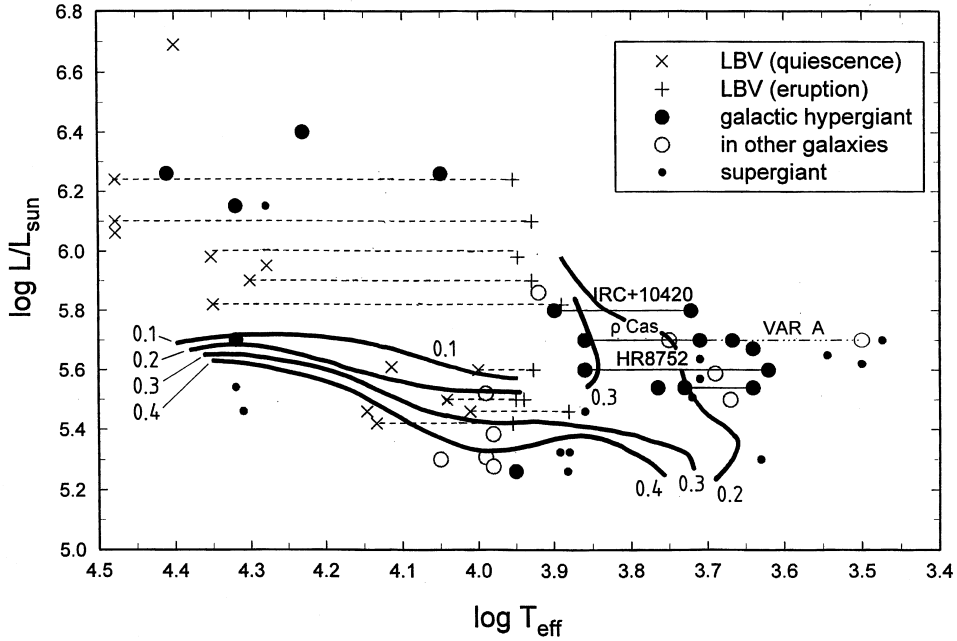

Figure 4. Lines of equal $\Delta r/R$-values in the upper HR diagram. Δr is the radial distance between the levels with $\tau_R = 0.001$ and 10; R is the stellar radius. The diagram is for the case $\zeta_\mu = 2v_s$.

REFERENCES

Blöcker T., Balega Y., Hofmann K.-H., Lichtenthäler J., Osterbart R., Weigelt G., 1999, A&A, 348, 805

Carpay J., de Jager C., Nieuwenhuijzen H., Moffat A., 1989, A&A, 216, 143

de Jager C., 1998, A&AR, 8, 145

de Jager C., Nieuwenhuijzen H., 1997, MNRAS, 290, L50

de Jager C., Nieuwenhuijzen H., van de Hucht K. A., 1988, A&AS, 72, 259

de Jager C., Lobel A., Israelian G., Nieuwenhuijzen H., 2001, in de Groot M., Sterken C., eds, ASP Conf. Ser. Vol. 233, P Cygni 2000, 400 years of progress. Astron. Soc. Pac., San Francisco, p. 191

El Eid M., Champagne A. E., 1995, ApJ, 451, 298

Humphreys R. M., 1975, ApJ, 200, 426

Humphreys R. M., 1978, ApJ, 219, 445

Humphreys R. M., Kudritzki R. P., Groth H. G., 1991, A&A, 245, 593

Israelian G., Lobel A., Schmidt M., 1999, ApJ, 523, L145

Jones T. J. et al., 1993, ApJ, 411, 323

Klochkova V. G., Chentsov E. L., Panchuk V. E., 1997, MNRAS, 292, 19

Lamers H. J. G. L. M., de Groot M., Cassatella A., 1983, A&A, 123, L8

Ledoux P., Flügge S. 1958, Handbuch d. Physik, Vol. 51. Springer, Heidelberg, p. 605

Lobel A., Israelian G., de Jager C., Musaev F., Parker J. Wm., Mavrogiorgou A., 1997, A&A, 330, 659

Maeder A., Meynet G., 1988, A&AS, 76, 411

Mutel R. L., Fix J. D., Benson J. M., Webber J. C., 1979, ApJ, 228, 771

Nieuwenhuijzen H., de Jager C., 1995, A&A, 302, 811

Nieuwenhuijzen H., de Jager C., 2000, A&A, 353, 163

Oudmaijer R. D., Geballe T. R., Waters L. B. F. M., Sahu K. C., 1994, A&A, 281, L33

Oudmaijer R. D., Groenewegen M. A. T., Matthews H. E., Blommaert J. A. D. L., Sahu K. C., 1996, MNRAS, 280, 1062

Ritter A., 1879, Wiedemann's Annalen der Physik u. Chemie, Vol. 8, p. 157

Stothers R., 1999, MNRAS, 305, 365

Stothers R., Chin C.-w., 1996, ApJ, 468, 842

Stothers R., Chin C.-w., 2001, ApJ, in press

Takeda Y., Takada-Hidai M., 1994, PASJ, 46, 395

van Genderen A. M., 2001, A&A, 366, 508

This paper has been typeset from a TEX/LATEX file prepared by the author.